

Yueqiang Liu, S.A. Sabbagh, I.T. Chapman, S. Gerasimov, Y. Gribov,
T.C. Hender, V. Igoshine, M. Maraschek, G. Matsunaga, M. Okabayashi
and E.J. Strait

Multi-machine Data Based Prediction of High-Frequency Sensor Signal Noise for Resistive Wall Mode Control in ITER

Enquiries about copyright and reproduction should in the first instance be addressed to the Culham Publications Officer, Culham Centre for Fusion Energy (CCFE), K1/083, Culham Science Centre, Abingdon, Oxfordshire, OX14 3DB, UK. The United Kingdom Atomic Energy Authority is the copyright holder.

Multi-machine Data Based Prediction of High-Frequency Sensor Signal Noise for Resistive Wall Mode Control in ITER

Yueqiang Liu^{1,2,3}, S.A. Sabbagh⁴, I.T. Chapman¹, S. Gerasimov¹, Y. Gribov⁵,
T.C. Hender¹, V. Igoshine⁶, M. Maraschek⁶, G. Matsunaga⁷, M. Okabayashi⁸,
and E.J. Strait⁹

¹ CCFE, Culham Science Centre, Abingdon, OX14 3DB, UK

² Southwestern Institute of Physics, PO Box 432, Chengdu 610041, China

³ Department of Earth and Space Science, Chalmers University of Technology, SE-412 96
Gothenburg, Sweden

⁴ Department of Applied Physics and Applied Mathematics, Columbia University, New York,
New York 10027, USA

⁵ ITER Organization, Route de Vinon sur Verdon, CS90046, 13067 St Paul Lez Durance Cedex,
France

⁶ Max Planck Institute for Plasma Physics, Boltzmannstr. 2, 85748 Garching, Germany

⁷ Japan Atomic Energy Agency, 801-1, Mukouyama, Naka, Ibaraki 311-0193, Japan

⁸ Princeton Plasma Physics Laboratory, Princeton, New Jersey 08543, USA

⁹ General Atomics, San Diego, California 92186, USA

Multi-machine data based prediction of high frequency sensor signal noise for resistive wall mode control in ITER

Yueqiang Liu^{1,2,3}, S.A. Sabbagh⁴, I.T. Chapman¹, S. Gerasimov¹, Y. Gribov⁵, T.C. Hender¹, V. Igoshine⁶, M. Maraschek⁶, G. Matsunaga⁷, M. Okabayashi⁸, and E.J. Strait⁹

¹CCFE, Culham Science Centre, Abingdon, OX14 3DB, UK

²Southwestern Institute of Physics, PO Box 432, Chengdu 610041, China

³Department of Earth and Space Science, Chalmers University of Technology, SE-412 96 Gothenburg, Sweden

⁴Department of Applied Physics and Applied Mathematics, Columbia University, New York, New York 10027, USA

⁵ITER Organization, Route de Vinon sur Verdon, CS90046, 13067 St Paul Lez Durance Cedex, France

⁶Max Planck Institute for Plasma Physics, Boltzmannstr. 2, 85748 Garching, Germany

⁷Japan Atomic Energy Agency, 801-1, Mukouyama, Naka, Ibaraki 311-0193, Japan

⁸Princeton Plasma Physics Laboratory, Princeton, New Jersey 08543, USA

⁹General Atomics, San Diego, California 92186, USA

Abstract. The high frequency noise measured by magnetic sensors, at levels above the typical frequency of resistive wall modes, is analyzed across a range of present tokamak devices including DIII-D, JET, MAST, ASDEX Upgrade, JT-60U and NSTX. Application of a high-pass filter enables identification of the noise component with Gaussian-like statistics, that shares certain common characteristics in all devices considered. A conservative prediction is made for ITER plasma operation of the high-frequency noise component of the sensor signals, to be used for resistive wall mode feedback stabilization, based on the multi-machine database. The predicted root-mean-square $n=1$ (n is the toroidal mode number) noise level is $10^4 - 10^5$ Gauss/second for the voltage signal, and 0.1-1 Gauss for the perturbed magnetic field signal. The lower cut-off frequency of the Gaussian pickup noise scales linearly with the sampling frequency, with the scaling coefficient of about 0.1. These basic noise characteristics should be useful for the modelling-based design of the feedback control system for the resistive wall mode in ITER.

1 Introduction

The resistive wall mode (RWM) [1] is a macroscopic instability that originates from the ideal external kink mode. Since the RWM causes a global, three-dimensional distortion of the plasma column [2], the onset of the mode, or sometimes even the strong response of a stable mode [3], often results in plasma disruption [4, 5]. Since the ITER 9MA steady state scenarios operate in the RWM regime (i.e. with the plasma pressure exceeding the Troyon no-wall beta limit), understanding as well as control of the mode becomes a key issue [4, 6, 7, 5]. As an example, the recent 9MA target plasma from the ITER design has $\beta_N = 2.93$, which is about half-way between the ideal MHD predicted no-wall ($\beta_N^{\text{nw}} \simeq 2.55$) and ideal-wall ($\beta_N^{\text{iw}} \simeq 3.55$) beta limits [8].

Both passive [1, 9, 10, 11, 12, 13, 14, 15, 16, 17, 18, 19, 20, 21, 22, 23, 24, 25, 26, 27, 28, 29, 30, 31] and active [32, 33, 34, 35, 37, 36, 38, 39, 40, 41, 42, 43, 2, 5, 44, 45, 47] control of the RWM has been extensively studied, in both theory and experiments. In particular, recent theory suggests that a strong drift kinetic damping of the RWM is possible, largely due to the precessional drift resonance of thermal particles [12, 15, 16, 17, 19]. On the other hand, kinetic modelling suggests that these damping effects may not provide a robust stabilisation of the RWM [48, 19, 50] over the full RWM regime, even in the presence of fusion born alphas [49, 19] as well as other fast ions [50]. Therefore, active control of the mode remains a desirable option for ITER [51]. A recent systematic study also suggests the possibility of synergistic effect between the passive (rotational stabilisation) and active (magnetic feedback) control [52].

To date most of the theory and modelling work on the RWM feedback neglected the influence of the disturbances and signal noise on the performance of the active control system, with few exceptions [53]. On the other hand, the measurement noise, which may come from many sources, can be detrimental to the performance of the control system. This effect can be taken into account by the control system, if the noise is quantified, which is the subject of this paper. Advanced control techniques, such as those based on the Kalman Filter, can easily account for the signal noise, especially that of Gaussian statistics. Therefore, for the purpose of direct modelling of the RWM control in ITER, it is necessary and desirable to specify the noise characteristics of the feedback control system.

In this work, which is also part of the activity within the framework of the International Tokamak Physics Activity (MHD Stability Topical Group), we consider specifically the sensor signal noise specification. In order to specify the noise characteristics in ITER, we generate a cross-machine database covering both conventional and low-aspect ratio tokamaks, as well as devices of various size. The devices considered here include DIII-D, JET, MAST, ASDEX Upgrade, JT-60U and NSTX. We try to extract common features of the high-frequency sensor signal noise with Gaussian statistics from the aforementioned devices, which we use for estimating the noise expected in the ITER feedback control system. The high-frequency range is defined as that exceeding the typical frequency of the resistive wall mode, which is in the order of 100Hz in most of the present day tokamak devices. We mainly consider the $n = 1$ Fourier decomposition of the magnetic sensor signals (which will be called the "n=1 sensor signal" throughout), with n being the toroidal mode number.

There can generally be many possible sources of the noise, from for example the plasma MHD activities, the parasitic pickup signals, the data acquisition hardware noise, the power supply noise, the electric motor noise, etc. The analysis of the noise characteristics can be associated with many aspects, and generally involves a few techniques. One aspect is how to separate the coherent signals from white noise. Generic choices include the usage of high-pass filtering to remove the low-frequency components of the signal, the usage of spectral analysis (FFT) to remove discrete, well defined frequencies, the application of the notch filter to remove the coherent components, etc. For a given time trace of the plasma discharge, it may also be possible to select time intervals where the coherent events (e.g. the edge localized modes (ELMs) or fishbone instabilities) are absent. The other aspect is the separation of the hardware induced noise from the plasma generated noise. So far there is no unique, superior procedure to filter such noise, partially due to the difficulty of designing filter/transfer functions to describe

the hardware noise. However, there are two special cases where the hardware noise can be easily separated. In the first case, one of the noise types is dominant, as in the vertical control analysis performed for JET [54]. In the second case, the hardware and the plasma noise signals have distinguishable frequency ranges.

In terms of the noise analysis methodology, we choose the two most common approaches, i.e. FFT analysis and Power Spectral Density (PSD) analysis. The latter is briefly discussed in the next Section, followed by a description of an analysis tool developed in this work. Section 3 reports the high frequency noise analysis results for each of the aforementioned tokamak devices. Section 4 shows the final cross-machine database from the noise analysis, and makes prediction for the noise characteristics in ITER. Section 5 summarises the work.

2 Analysis tool

2.1 A brief introduction to PSD analysis

Consider a (generally complex) time series signal $s(t)$. The PSD is defined as

$$S(f) \equiv \lim_{T \rightarrow \infty} E \left[\left| \frac{1}{\sqrt{T}} \int_0^T s(t) e^{-i\omega t} dt \right|^2 \right], \quad (1)$$

where $E[\cdot]$ is the mean value, $\omega = 2\pi f$. We list a few interesting properties of the PSD for a stationary random signal.

1. Because the mean value is taken, $S(f)$ is a smooth f(i.e. not noisy) function of frequency f , even for a noisy signal $s(t)$. This property is useful for accurate determination of certain quantities such as the signal bandwidth.
2. PSD satisfies the Wiener-Khinchin Theorem

$$S(f) = \int_{-\infty}^{\infty} E[s(t)s^*(t+\tau)] e^{-i\omega\tau} d\tau, \quad (2)$$

where $E[s(t)s^*(t+\tau)]$ is the autocorrelation function for signal $s(t)$.

3. For real signal $s(t)$, $S(-f) = S(f)$ (even function); for complex signal $s(t)$, $S(-f) = S^*(f)$ (Hermitian function).
4. $S(f) = \langle |\text{FFT}[s(t)]|^2 \rangle$, where $\langle \cdot \rangle$ means average over many sample signals with the same characteristics.
5. The averaged power of PSD is equal to the root-mean-square (RMS) of the signal.
6. If the function $P(f) = \left(\int_0^f S(f) df \right)^{1/2}$ saturates at certain frequency $f = B$, B corresponds to the bandwidth of the signal $s(t)$.

In this work, we shall employ some of the aforementioned properties to compare the noise characteristics from different machines, as well as to extract global parameters (such as the RMS and the bandwidth) for the noise specification.

2.2 Butterworth high-pass filter for the noise data analysis

To characterise the high-frequency part of the signal from experimental measurements, we use a high-pass filter of the Butterworth type. The Butterworth filter is known for its maximally flat frequency response (in terms of amplitude) in the passband. Compared to other filters such as the Chebyshev or elliptic types, a Butterworth filter does not exhibit the issue of amplitude ripple in the passband or the stopband. However, it does have a slower roll-off in the frequency response.

For our purpose, we require no more than 2 decibel (dB) loss in the passband, and at least 40dB attenuation in the stopband. We also tune the edge frequencies of the stop- and pass-bands to obtain the filtered noise signal which has as close as possible a Gaussian-like probability distribution function (pdf). We find that a 7-th order Butterworth filter can satisfy our requirements, for most of the experimental data (DIII-D, JET, MAST, ASDEX Upgrade, JT-60U, NSTX) that we analysed, with an edge frequency of the stopband $\omega_s = 0.125$ (normalised from 0 to 1 where 1 corresponds to π radians/sample), and the passband edge frequency $\omega_p = 0.25$. The filter reads

$$y(n) = \sum_{i=1}^{N+1} b_i x(n-i+1) - \sum_{i=2}^{N+1} a_i y(n-i+1), \quad (3)$$

where $x(n)$ is the time series of the raw signal, and $y(n)$ is the filtered signal. The filter has an order $N = 7$, with the coefficients listed in Table 1. Figure 1 shows the Bode plot of the frequency response of this high-pass filter.

Table 1: The coefficients for the Butterworth filter.

i	1	2	3	4	5	6	7	8
a_i		-3.7136	6.3804	-6.4045	4.0127	-1.5577	0.3452	-0.0336
b_i	0.1832	-1.2823	3.8469	-6.4114	6.4114	-3.8469	1.2823	-0.1832

2.3 Noise signal analysis tool (NSAT)

We have developed a simple suite of Matlab scripts, in order to perform the signal analysis carried out in this work. This Matlab suite (called NSAT) contains commands for generating the aforementioned Butterworth filter, as well as other filters and FFT tools. NSAT also performs PSD analysis of the signal, builds the pdf of the raw and the filtered signals. For the filtered signals, the scripts calculate the root-mean-square value, defined as the standard

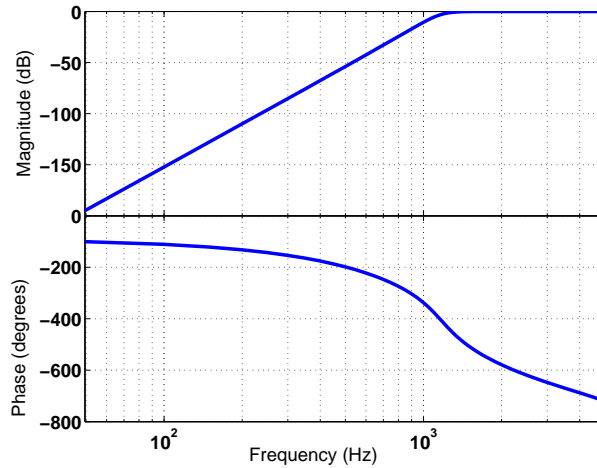


Figure 1: Bode plot of 7-th order Butterworth high-pass filter used in the signal data noise analysis.

deviation of the noise signal. Two characteristic frequencies are defined and extracted based on PSD analysis, as shown in the examples below.

This tool allows us to analyse the magnetic measurements data from various devices on the same basis. In the following, we perform the signal data analysis from various present tokamak machines using NSAT. In all the cases, we consider the $n = 1$ signal (which is often obtained after numerical processing of the raw sensor data) unless stated otherwise.

3 Multi-machine data analysis

3.1 Magnetic pickup coils on various devices

Table 2 lists certain basic characteristics of pickup coils used in various devices. The noise data collected by these pickup coils will be analysed in the following Subsections, for each individual device, and summarised in Subsection 4.1.

There can generally be various possible sources for the sensor signal noise, for instance the noise in the instrumentation (the integrators, amplifiers, and the analogue-to-digital converters), the magnetic power supply noise (coupled from the magnetic coils and leads), and the plasma generated noise (MHD modes and turbulences). In order to distinguish these sources of noise, we try to analyse and compare the sensor data from vacuum shots with the magnetic coils on or off (denoted by “Vac” and “Vac+Coil”, respectively, in Table 3), and from discharges with plasmas. Here the term “coils” specifically refers to the 3D coils that produce $n \neq 0$ magnetic field perturbations. The “vacuum shots” refer to cases where these 3D coils are switched off; however, for all the cases analyzed here, the 2D equilibrium coils are switched

Table 2: Characteristics of magnetic sensors on various devices.

device	sensor	component	location	sample time [ms]	linkage area/turn [cm ²]
DIII-D	pickup	b_p	LFS	0.005	600
DIII-D	pickup	b_p	LFS	0.1	620
JET	saddle	b_r	LFS&HFS	0.2/0.4/13.8	2.3×10^4
MAST	saddle	b_r	HFS	0.0025/0.004	6.5
ASDEX Upgrade	saddle	b_r	HFS	0.1	1.4×10^4
JT-60U	saddle	b_r	LFS	0.002	7.5×10^4
JT-60U	pickup	b_p	LFS	0.002	120
NSTX	saddle	b_p	LFS	0.2	76.3

Table 3: Types of the analysed discharges on various devices.

device	Vac	Vac+Coil	Low	Low+Coil	High	High+Coil
DIII-D			✓	✓	✓	✓
JET	✓	✓	✓	✓	✓	✓
MAST	✓	✓			✓	✓
ASDEX Upgrade	✓		✓	✓	✓	✓
JT-60U			✓		✓	
NSTX		✓		✓		✓

on. The plasma discharges are further classified into the low beta (denoted as “Low”) and high beta (“High”) regimes, with each regime having coils on or off. The choice of the above clarification is based on an heuristic understanding of the plasma beta effect on the (plasma generated) noise level. Note that low beta plasma does not necessarily correspond to a stable RWM (one example is the current driven RWM at low beta). Similarly, high beta plasma does not necessarily correspond to an unstable RWM - the mode may be stabilized by a strong kinetic damping. Not all the above described data are available on each of the six devices that we choose to analyse. The types of discharges that we have analysed in this work are summarized in Table 3.

In the following, we show only selected examples (discharges) of the sensor data analyse results on each of the devices, with a brief summary of the results for the remaining discharges as listed in Table 3. The full analysis of the results is found in a comprehensive report [55].

3.2 Sensor signal noise analysis for DIII-D data

Both radial and poloidal fields data are available in DIII-D. The examples shown below are based on the poloidal field data measured by pickup coils. The raw data are in Gauss/second. We shall first analyse the spectrum of the raw data, followed by the analysis for the time

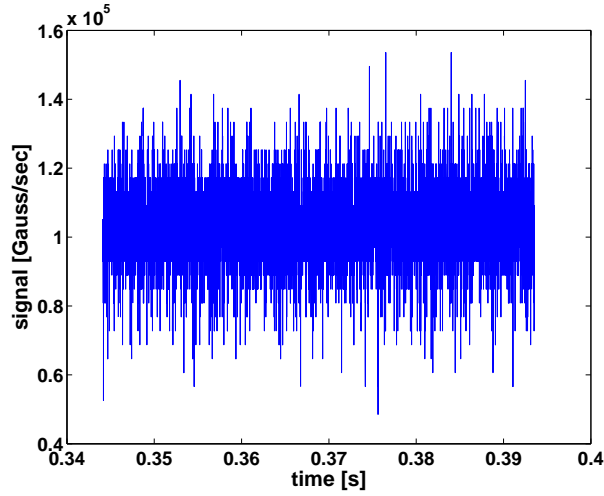


Figure 2: Example of the raw pickup coil signal (the combined $n = 1$ signal without filtering) from DIII-D 133012 with current driven RWM.

integrated data (for the perturbed field).

3.2.1 Analysis of raw measured field variation data (voltage signals)

We have analysed the sensor signal data from 4 different types of discharges. One example from a low beta current driven RWM experiment is shown below. The raw pickup coil data, in Gauss/sec, is plotted in Fig. 2 for the time period of 344-394ms, with the sampling time of $5\mu\text{s}$. The RWM feedback using the $n = 1$ sensor measurement and an $n = 1$ applied field as an actuator is activated for this shot.

Figure 3 shows the NSAT analysis results for this raw voltage data, using the Butterworth high-pass filter described in Section 2.2. The filtered signal has a pdf which is close to Gaussian noise, as shown by dots in Fig. 3(b). Here the pdf is built using a histogram with 100 equally spaced bins. The signal itself is normalized by the maximal span of the data values. The distribution function is normalized such that the total probability is equal to unity. The standard deviation, or the RMS, is $8.64 \times 10^3 \text{ Gauss/second}$. This same RMS value is used to construct an exact Gaussian distribution (with the total probability of 1), which is plotted as the dashed line curve in Fig. 3(b).

Figure 3(c) shows the amplitude of the FFT spectrum (simply denoted as $|\text{FFT}|$) for the filtered signal shown in (a), versus the frequency. From Fig. 3(d), we also define two characteristic frequencies. One is the lower band cut-off frequency below which the FFT and PSD are approximately zero. This frequency, which is further referred to as band 1, is estimated to be about 16kHz for this signal. The other frequency, called band 2, corresponds to the first peak of the PSD, and is about 30kHz for this signal. The information presented by Fig. 3 show some of the most important features of the noise signal under consideration. We shall use the same type of plots to display the noise characteristics from other DIII-D discharges, as well as

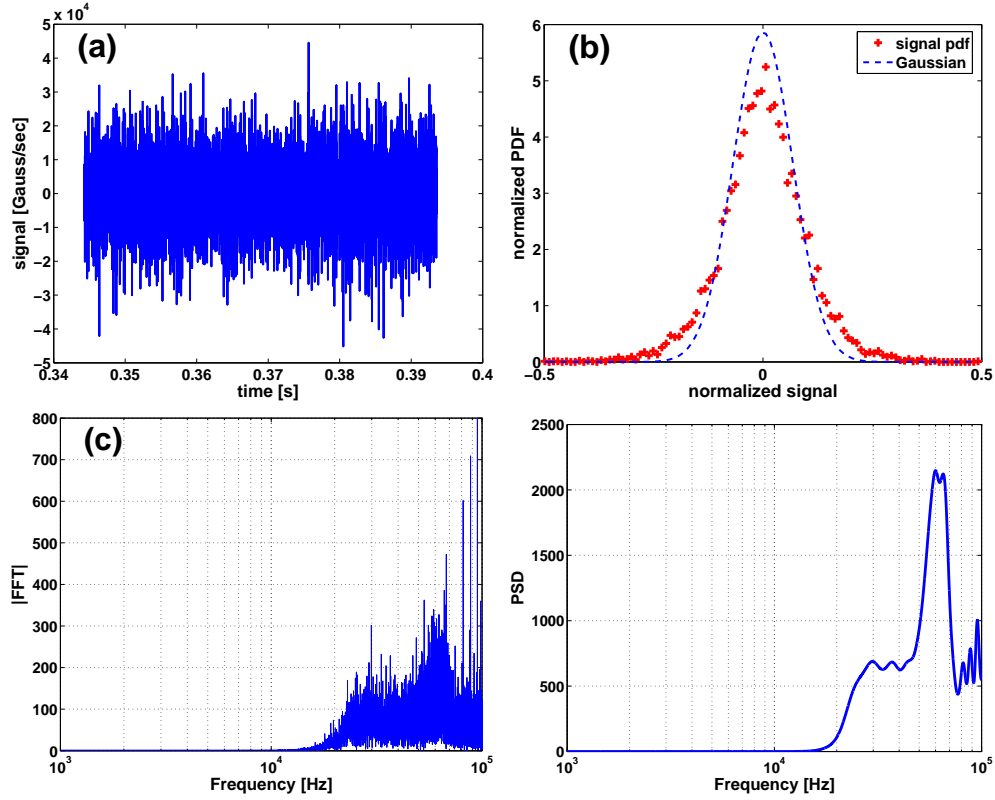


Figure 3: Characteristics of the noise signal after applying the Butterworth high-pass filter to the raw pickup coil signal shown in Fig. 2 (shot 133012): (a) the time series of the filtered signal, with the sampling time of $5\mu\text{s}$, (b) the normalised probability distribution function ('+') compared with a Gaussian pdf (dashed line) with the same RMS, (c) the FFT spectrum and (d) the power spectral density of the filtered signal.

from other devices later on. Before proceeding further, we point out that the band 1 and 2, that we define here, depends on the choice of the high-pass filter, in particular, on the passband (ω_p) and stopband (ω_s) of the Butterworth filter. However, for a fixed choice of filter, as we follow here, these two bands are well defined, and as we shall show, they scale well with the sampling frequency of the raw signal.

The same analysis has been applied to other DIII-D low beta plasmas that are subject to current driven RWMs. The discharge that we considered are: 133020, 133021 (no feedback), 133011-133014 (feedback with various proportional gains). In summary, the RMS of the filtered high-frequency noise varies between 6.8×10^3 and 1.2×10^4 Gauss/second. The values of band 1 and 2, respectively, are close to that of the example shown in Fig. 3.

Similar analysis is also made for a high beta ($\beta_N \sim 3.5$) discharge 147410. No feedback is applied to the RWM in this discharge. Since there are bursting events during the discharge, we choose time periods between the bursting events for the noise analysis. In general, the RMS varies between 1.0×10^5 and 3.9×10^5 Gauss/second for this discharge, more than one order of magnitude higher than the low beta case shown in Fig. 3.

Another high beta ($\beta_N \sim 3.5$) discharge (147626) also includes the RWM feedback stabilization with a proportional-integral-derivative (PID) controller, and with a response time of 1ms. Notably, by examining various time periods between the bursting events, we find that the RMS varies between 3.1×10^4 and 7.6×10^4 Gauss/second for this discharge.

For a similar high beta plasma, a faster feedback with 0.1ms response time, is also applied in experiments. One such case is shot 147406. We find that the RMS varies between 4.2×10^4 and 4.6×10^5 Gauss/second. With the more responsive feedback, the RMS level is somewhat higher, but remains in the similar range for the above two examples. All the above results (RMS, band 1 and 2) will be summarised in a later figure, together with data collected from other devices.

3.2.2 Analysis of integrated measurements (magnetic field signals)

In this section, the raw pickup coil signals shown in the previous Subsection are time integrated (using both hardware and software) to give a magnetic field measurement, and then filtered using the Butterworth high-pass filter described in Section 2.2. The filtered signal, as well as its spectral characteristics are again processed by NSAT, for the same 4 cases analysed before, respectively. For the low beta case shown in Figs. 4, the filtered signal again has pdf which is close to a Gaussian noise. The standard deviation is 0.022G.

Applying the same analysis to other DIII-D low beta plasmas with current driven RWM, we find that the RMS of the filtered high-frequency noise varies between 0.019G and 0.028G. The values of band 1 and 2, respectively, are close to that of the example shown in Fig. 4.

We mention that, for these low beta plasmas, hardware integrated signals are also available, with pickup coils measuring the b_p signal at a sampling time of 0.1ms. Applying the same filtering procedure to these signals, we find a similar RMS level.

For the high beta ($\beta_N \sim 3.5$) no-feedback discharge, the RMS varies between 0.5G and 3G for this discharge, more than one order of magnitude higher than the low beta case shown in Fig. 4.

For the 1ms feedback-on, high beta ($\beta_N \sim 3.5$) discharge 147626, the NSAT analysis results show that the RMS varies between 0.1G and 0.3G. This RMS level is again lower than the case without feedback, similar to the corresponding voltage signal. For shot 147406 with 0.1ms feedback, The RMS, for different time periods, varies between 0.2G and 2G.

3.3 Sensor signal noise analysis for JET data

In JET, the external error field correction coils (EFCC) are used to excite the resonant field amplification (RFA) response and to probe the beta limits of high beta plasmas [29]. The $n = 1$ EFCC current configuration is considered in the examples shown below. The plasma response

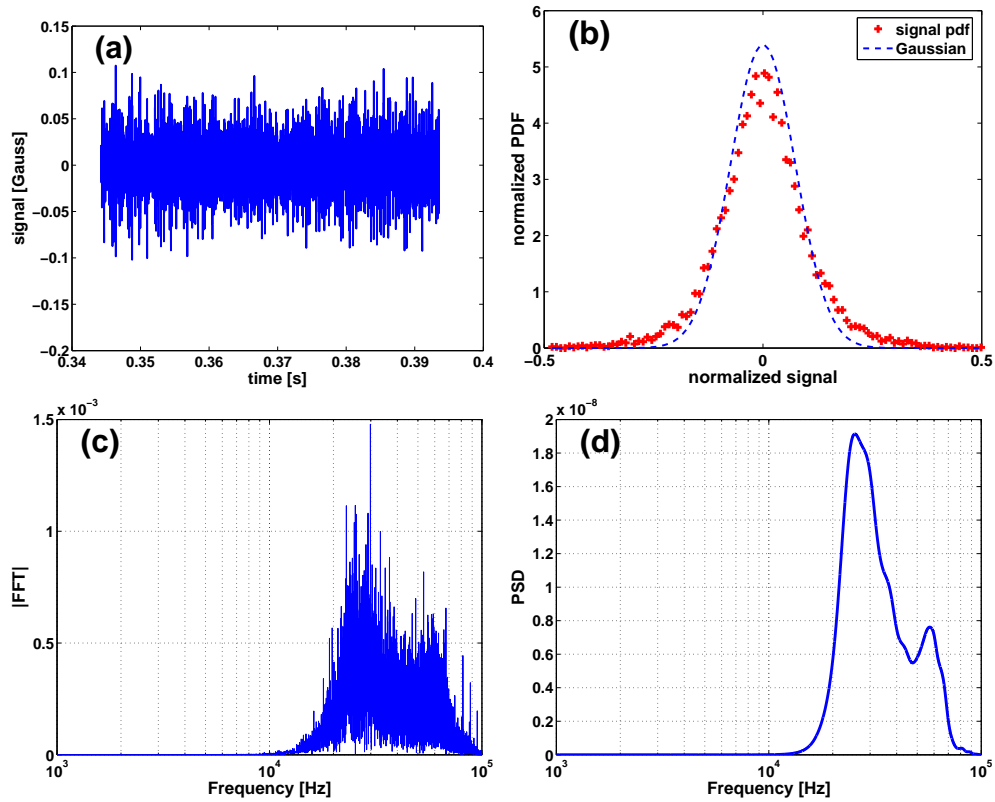


Figure 4: Characteristics of the noise signal after applying the Butterworth high-pass filter to the time integrated pickup coil signal shown in Fig. 2 (shot 133012): (a) the time series of the filtered signal, with the sampling time of $5\mu\text{s}$, (b) the normalised probability distribution function ('+') compared with a Gaussian pdf (dashed line) with the same RMS, (c) the FFT spectrum and (d) the power spectral density of the filtered signal.

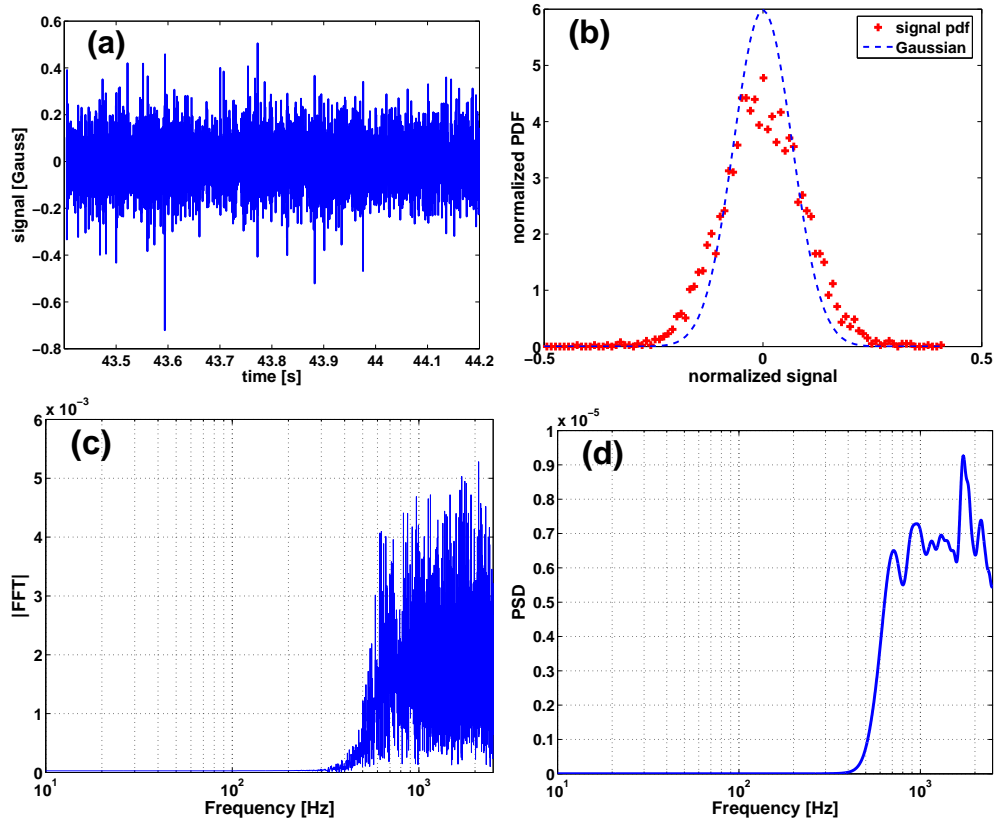


Figure 5: Characteristics of the noise signal after applying the Butterworth high-pass filter to the MHDG sensor signal from JET discharge 62024: (a) the time series of the filtered signal, with the sampling time of 0.2ms, (b) the normalised probability distribution function ('+') compared with a Gaussian pdf (dashed line) with the same RMS, (c) the FFT spectrum and (d) the power spectral density of the filtered signal.

is measured by the low-field-side (LFS) pickup coils with a large area ($\sim 2.3\text{m}^2$ per coil) [56]. These pickup coils measure the amplitudes of the normal field component variation just outside the vacuum vessel. The constructed $n = 1$ sensor signals can be either 90° toroidally phase shifted w.r.t. the applied EFCC current (MHDG-signal), or in phase with the EFCC current (MHDF). In general, the signal sampling rate can be controlled in experiments. The present day standard set-up is 5kHz (0.2 ms) across the pulse, with the possibility of increasing the sampling rate up to 200kHz for non-integrated signals. For the discharges analysed in this work, three sampling times were used: 0.2ms, 0.4ms and 13.8ms.

Figure 5 shows one example of the filtered MHDG-signal, at the sampling rate of 5kHz, from the JET discharge 62024 during the high beta phase ($\beta_N \sim 2.5$). The same Butterworth filter as that used for the DIII-D data analysis is applied here. The RMS of the noise is about 0.1G for this example. We also examined the low-beta phase of this discharge, and periods with the EFCC on and off. In addition, the data from another high beta discharge 59223 is also analysed. In general, the RMS of the filtered signal varies between 0.1G and 0.15G in all of these discharges.

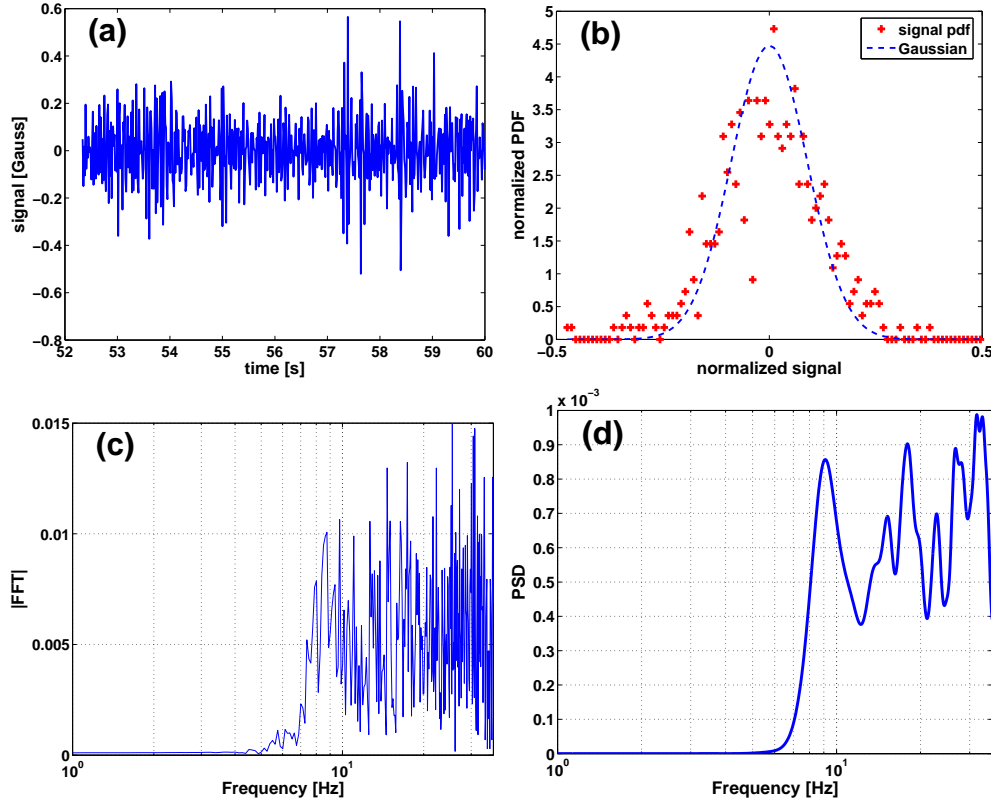


Figure 6: Characteristics of the noise signal after applying the Butterworth high-pass filter to the MHDG sensor signal from JET discharge 62024: (a) the time series of the filtered signal, with the sampling time of 13.8ms, (b) the normalised probability distribution function ('+') compared with a Gaussian pdf (dashed line) with the same RMS, (c) the FFT spectrum and (d) the power spectral density of the filtered signal.

The RMS of the noise in JET does not seem to be sensitive to the signal sampling time either. Figure 6 shows another example from the same JET discharge 62024, but the data are measured during another time period (low beta phase), and the sampling time is 13.8ms. Despite this, the noise RMS is in the same range between 0.1G and 0.15G. The bandwidth of the noise signal is obviously rather different.

The lack of sensitivity of the noise on the plasma conditions in JET indicates that the signal noise probably comes from the hardware. The most likely source is the analogue-to-digital converters (ADC). Nevertheless, the noise level in JET is not far from that of the DIII-D high beta plasmas.

3.4 Sensor signal noise analysis for MAST data

The MAST plasmas have much smaller aspect ratio compared to JET and DIII-D, and (generally) much higher β_N values. For the example shown in Fig. 7, the peak β_N is 4.8. Small

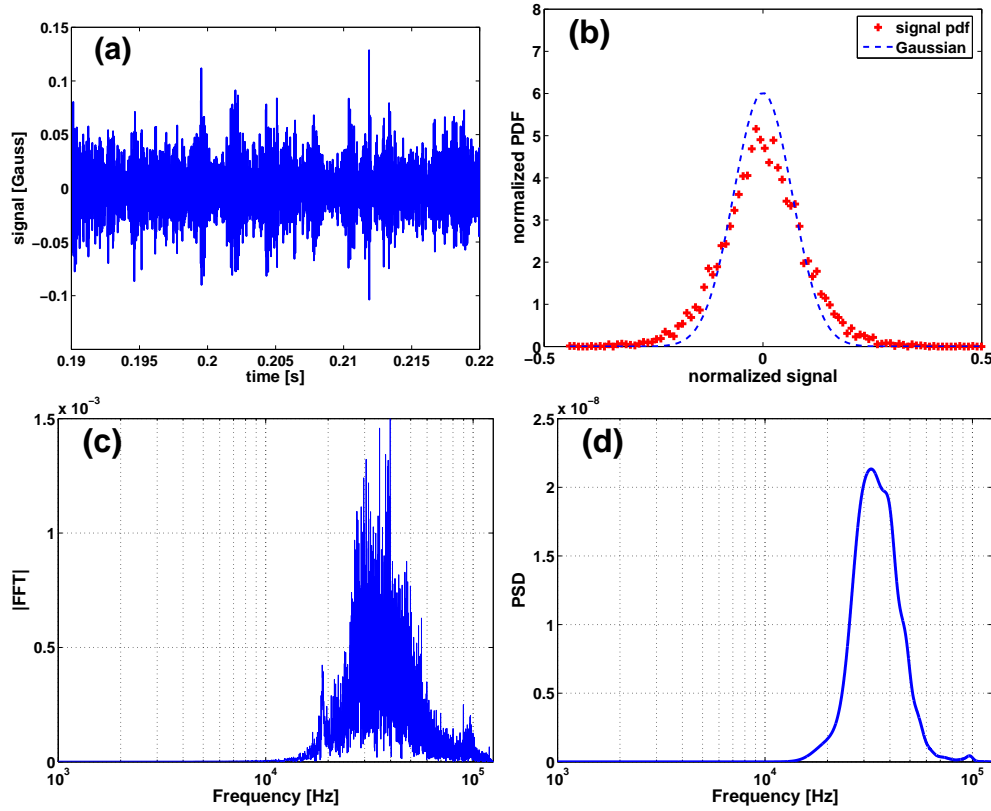


Figure 7: Characteristics of the noise signal after applying the Butterworth high-pass filter to the sensor signal in MAST discharge 25104: (a) the time series of the filtered signal, with the sampling time of $4\mu\text{s}$, (b) the normalised probability distribution function ('+') compared with a Gaussian pdf (dashed line) with the same RMS, (c) the FFT spectrum and (d) the power spectral density of the filtered signal.

saddle loops are used to measure the radial field perturbations at the high field side of the torus (Table 2). The sampling time of the sensor signal is $4\mu\text{s}$. We choose a time period of 30ms to perform the high-pass filtering. [The signal is not always stationary for a long period of time in this high beta discharge, probably due to the presence of coherent MHD events.] The RMS for the noise shown in figure is 0.02G. By examining the other high beta phase time periods, as well as other high beta discharges (25109 with peak $\beta_N \sim 3.3$, 25112 with peak $\beta_N \sim 4.4$, 25105 with peak β_N exceeding 5) we find that the RMS of the high-frequency noise in MAST varies between 0.01G and 0.1G.

On the other hand, the vacuum shots in MAST produces rather low level noise. One example is shown in Fig. 8, where a 20Hz in-vessel ELM control coil current is applied during the (vacuum) discharge (for the testing purpose). The filtered signal, at $2.5\mu\text{s}$ sampling time, has sub-mG (between 0.3mG and 1mG) noise level. The same observation holds also for pure vacuum shot (24613) without coils. We note that the filtered sensor signal shown in Fig. 8 does not well follow Gaussian pdf. This is partially related to the two constraints that we impose for constructing the analytic Gaussian distribution function shown by the dashed line. One is the requirement of exact matching of the standard deviation, to that of the filtered sensor data.

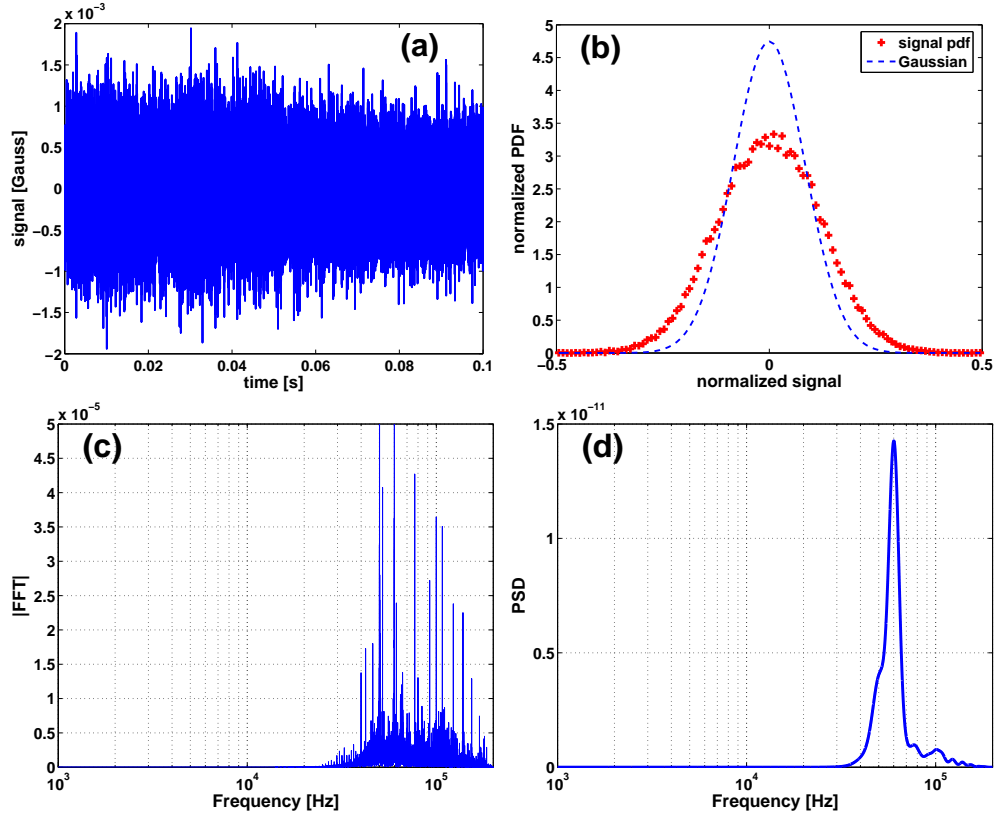


Figure 8: Characteristics of the noise signal after applying the Butterworth high-pass filter to the sensor signal in MAST discharge 24629: (a) the time series of the filtered signal, with the sampling time of $2.5\mu\text{s}$, (b) the normalised probability distribution function ('+') compared with a Gaussian pdf (dashed line) with the same RMS, (c) the FFT spectrum and (d) the power spectral density of the filtered signal.

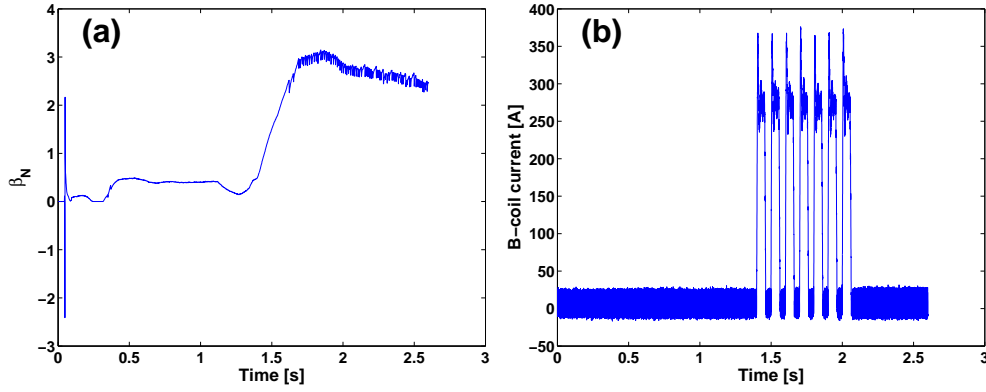


Figure 9: Time traces of ASDEX Upgrade high beta RFA pulse 27929 for (a) the normalised pressure β_N and (b) the B-coil current.

The second is the conservation of the total probability (to be unity). Relaxing these constraints may result in a better fitting of the data, but this is not the purpose of constructing Gaussian pdf here. Even without the relaxation of the aforementioned two constraints, it is still possible to obtain a better Gaussian-like pdf for the filtered signal, if we further tune the pass- and stop bands of the Butterworth filter for this specific example. However, for the purpose of achieving a uniform treatment of the sensor data from all devices, we choose to apply exactly the same filter for all data.

3.5 Sensor signal noise analysis for ASDEX Upgrade data

The raw ASDEX Upgrade data are in [V]. We have converted these data to [Gauss/second] by dividing the raw data by the area of the saddle loops in ASDEX Upgrade.

3.5.1 Analysis of the voltage signals

In ASDEX Upgrade, the B-coils (upper and lower coil sets inside VV) are powered to produce short time current blips, in order to probe the plasma response during the high beta phase of the discharge. One example is shown in Fig. 9.

A pair of large saddle coils, located at the high-field-side (HFS) of the torus, is used to measure the plasma response. We again apply the same noise analysis tool to these ASDEX Upgrade plasmas (discharge 27929 with peak $\beta_N = 2.9$, 27930 with peak $\beta_N = 3.8$, 27931 with peak $\beta_N = 3.8$). One example is shown in Fig. 10 for discharge 27929 during the time duration period of 2.1-2.6s. Examining various cases (coil current on/off, low to high beta phases), we find that the noise RMS is not sensitive to β_N nor to the coil currents. The RMS of the voltage signal noise varies between 6.0 and 10.6 Gauss/second, which is about 3-4 orders of magnitude lower than that of the DIII-D pickup coil signal. We attribute this difference to the

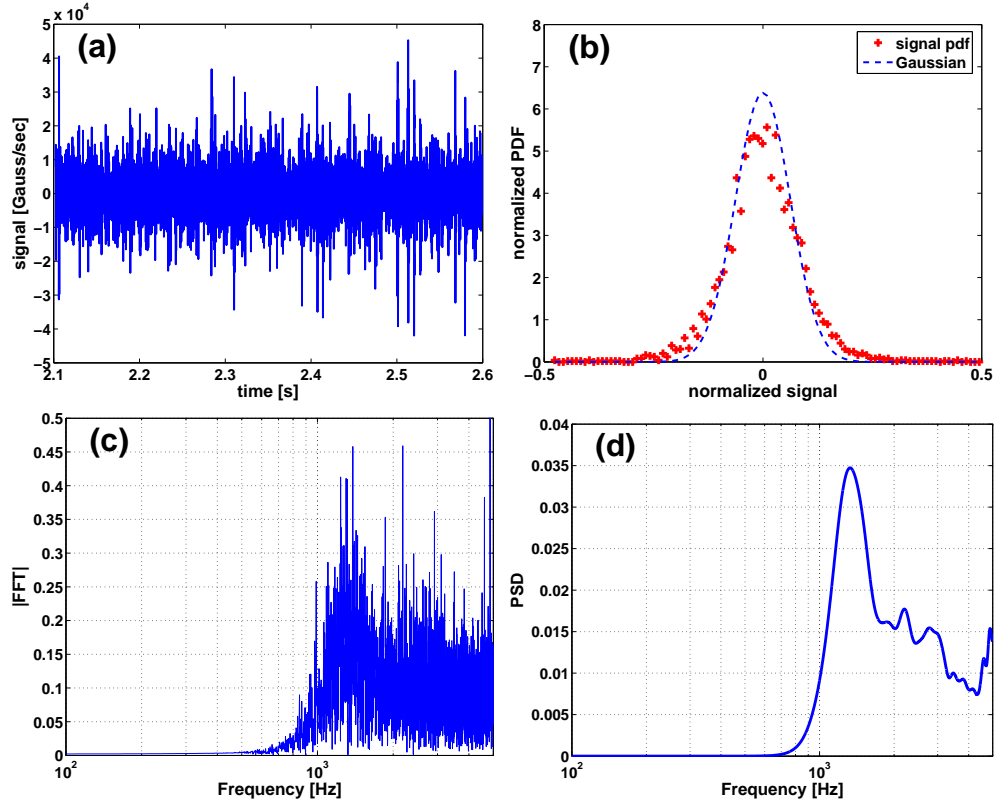


Figure 10: Characteristics of the noise signal after applying the Butterworth high-pass filter to the voltage sensor signal in ASDEX Upgrade discharge 27929: (a) the time series of the filtered signal, with the sampling time of 0.1ms, (b) the normalised probability distribution function ('+') compared with a Gaussian pdf (dashed line) with the same RMS, (c) the FFT spectrum and (d) the power spectral density of the filtered signal.

significantly larger pickup coil's area in ASDEX Upgrade, than the pickup coils in DIII-D, as well as the fact that the ASDEX Upgrade saddle loops measure the data at the high field side of the torus.

3.5.2 Analysis of the field signals

The corresponding time integrated signal is shown in Fig. 11 for discharge 27929 during the time period of 2.1-2.6s. Examining various cases (coil current on/off, low to high beta phases) again shows that the noise RMS, in Gauss, is not sensitive to β_N nor to the coil currents.

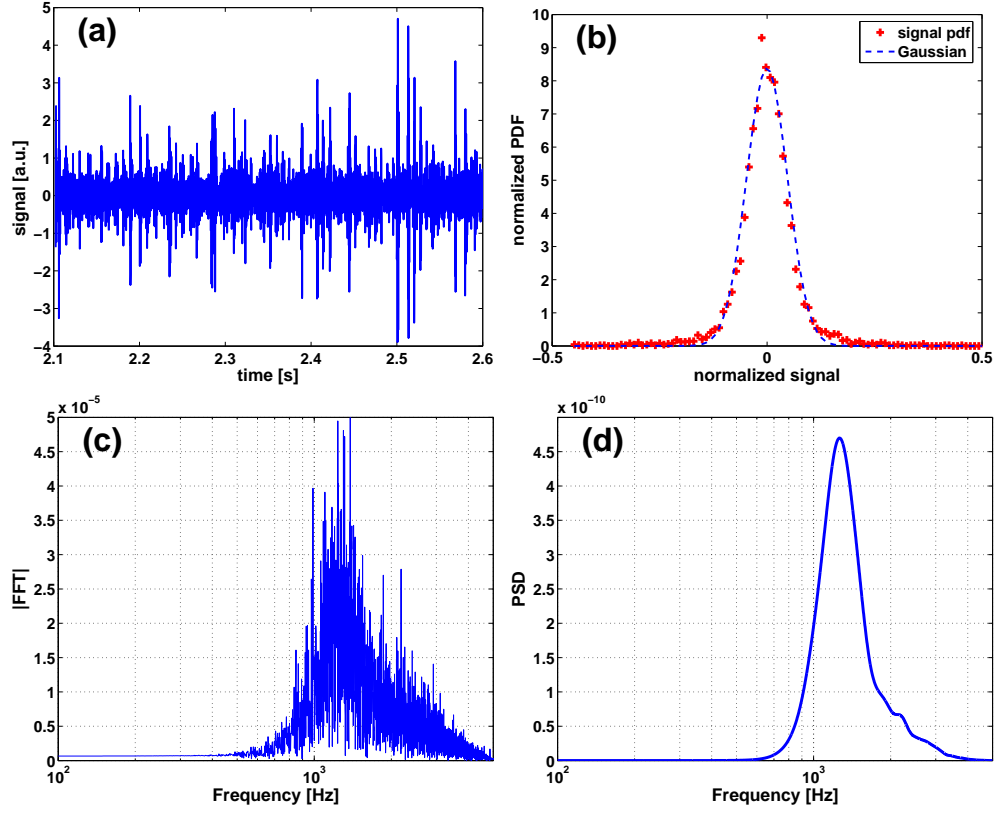


Figure 11: Characteristics of the noise signal after applying the Butterworth high-pass filter to the time integrated sensor signal in ASDEX Upgrade discharge 27929: (a) the time series of the filtered signal, with the sampling time of 0.1ms, (b) the normalised probability distribution function ('+') compared with a Gaussian pdf (dashed line) with the same RMS, (c) the FFT spectrum and (d) the power spectral density of the filtered signal.

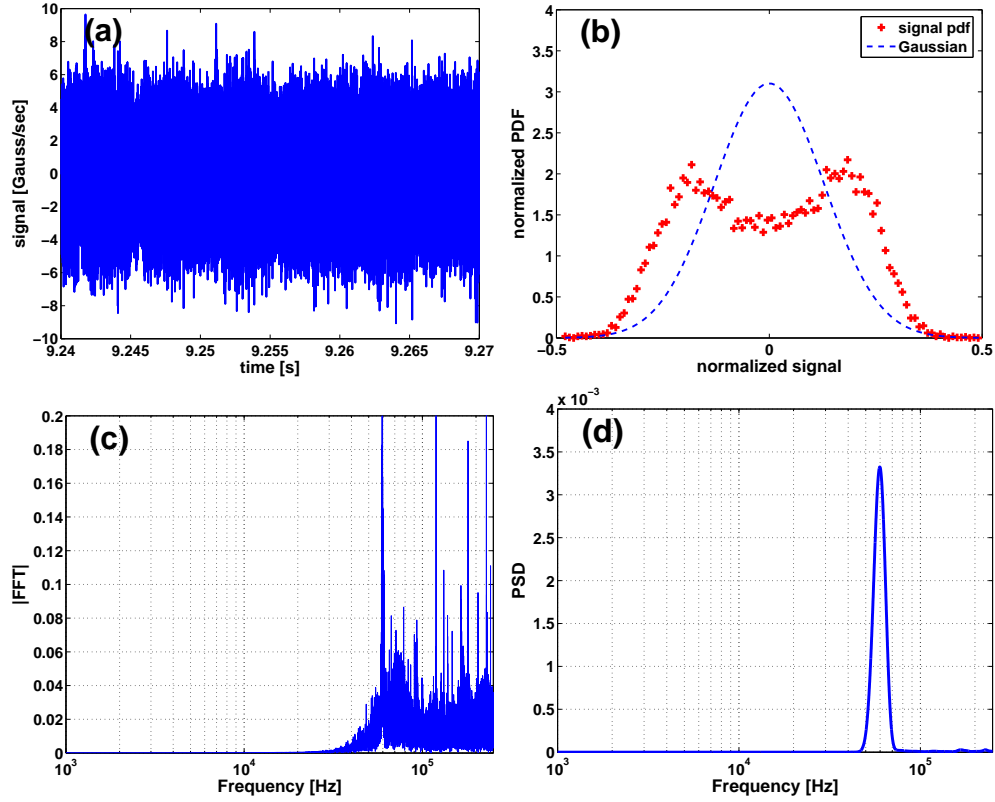


Figure 12: Characteristics of the saddle loop noise after applying the Butterworth high-pass filter to the voltage sensor signal in JT-60U low beta discharge 48710: (a) the time series of the filtered signal, with the sampling time of $2\mu\text{s}$, (b) the normalised probability distribution function ('+') compared with a Gaussian pdf (dashed line) with the same RMS, (c) the FFT spectrum and (d) the power spectral density of the filtered signal.

3.6 Sensor signal noise analysis for JT-60U data

The JT-60U data are available as the voltage signals in Gauss/second. We have analysed two types of discharges, with low (current driven RWM) and high (pressure driven RWM) plasma pressures, respectively. In both cases, the magnetic perturbations, in [Gauss/second], are measured by saddle loops (for the radial field), and by pickup coils (for poloidal field). The saddle loops are mounted inside, and very close to, the vacuum vessel. The sampling time for both type of coils is $2\mu\text{s}$. In JT-60U, there are multiple saddle loops along the toroidal angle, allowing the construction of the $n = 1$ field, which is shown in Fig. 12. However, the pickup coils are located at many toroidal angles with irregular spacing. Therefore, the noise analysis for the poloidal field component is carried out for the raw signal, without Fourier decomposition along the toroidal angle.

The high-frequency noise level from the saddle loops is low in JT-60U and comparable to that the ASDEX Upgrade saddle loop data, for both low and high beta plasmas. For the signals shown in Figs. 12 (the low beta case), the RMS is 7.94 Gauss/second. This noise level varies little during the other time periods of the discharge. The saddle loop noise is about 5 times

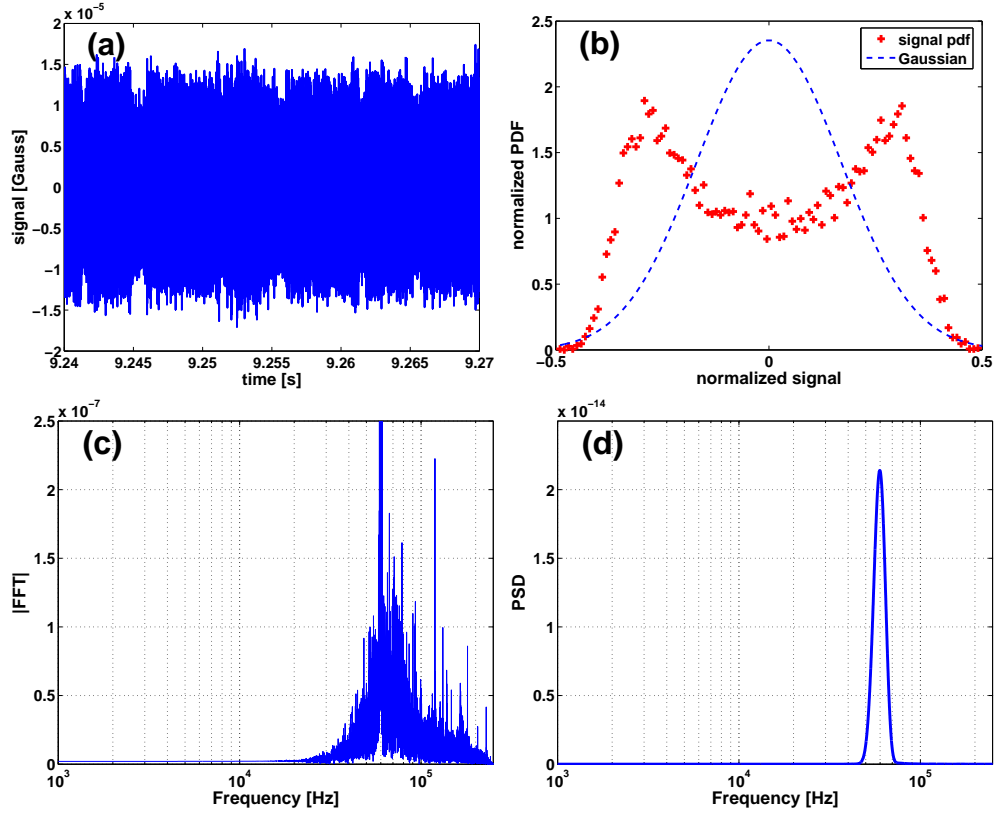


Figure 13: Characteristics of the saddle loop noise after applying the Butterworth high-pass filter to the field sensor signal in JT-60U low beta discharge 48710: (a) the time series of the filtered signal, with the sampling time of $2\mu\text{s}$, (b) the normalised probability distribution function ('+') compared with a Gaussian pdf (dashed line) with the same RMS, (c) the FFT spectrum and (d) the power spectral density of the filtered signal.

higher in the high beta plasma case.

As expected, the noise level is considerably higher for the pickup coil signals. For the same time period as shown in Fig. 12, the pickup coil signal noise RMS, for this low beta discharge, is $4.83 \times 10^3 \text{ Gauss/second}$. For the high beta case, the pickup coil signal noise level is even higher, by a factor of about 10.

We also note that, whilst the filtered signal is close to a Gaussian distribution for the pickup coil signal (in fact for both low and high beta cases), the signal has a more window-shaped distribution (i.e. close to a white noise) for the filtered saddle loop data at low beta (the high beta case, not shown here, again has a Gaussian-like distribution).

For the analysis of the field signals, we time-integrate the raw voltage signal to obtain the data in [Gauss], for both the low beta case shown in Fig. 13, and the high beta plasma case. The saddle loop (Fig. 13) signal is shown here.

Similar to the voltage signal, the high-frequency noise level from the saddle loops, for the

magnetic field, is very low in JT-60U, for both low and high beta plasmas. For the signals shown in Figs. 13 (the low beta case), the RMS is 1.94×10^{-5} Gauss. This noise level again remains almost constant during the other time periods of the discharge. The saddle loop noise is about 5 times higher in the high beta plasma case. This level is still about 3 orders of magnitude lower than the JET saddle loop data, which is probably predominantly contributed by the hardware noise.

As expected, the noise level is considerably higher for the pickup coil signals. For the same time period as shown in Fig. 13, the pickup coil signal noise RMS, for this low beta discharge, is 5.14×10^{-3} Gauss. For the high beta case, the RMS is again higher by an order of magnitude.

3.7 Sensor signal noise analysis for NSTX data

NSTX has extensive experimental data accumulated that utilizes active RWM feedback control, including very high normalized beta values exceeding 7 and toroidal beta up to 40% [20]. The sensor signals from both vacuum shots and RWM feedback shots at high beta are available. The data at high beta plasmas include various plasma conditions, feedback configurations, and MHD mode activities.

We have analysed and compared the $n = 1$ sensor signal (the perturbed magnetic field, with the measured signal integrated in hardware) used in the RWM control experiments, from two vacuum shots and three high beta shots. All the sensor data were obtained with a sampling time of 0.2ms. For the vacuum discharge 131610, the field switching power amplifier (SPA1-3) is applied with dc RWM coil current as well as ac frequency sweep. The RMS of the $n = 1$ noise for this shot is 0.444G.

In another vacuum shot (136181), the full (equilibrium) 2D fields are also included, together with staggered 3D field SPA1-3 and the coil current ramp up/down. The high frequency noise level is 0.431G, similar to shot 131610, but with somewhat less peaks in both FFT and PSD spectra.

Figure 14 shows a high beta case where the RWM is stabilised by the feedback system using proportional gain and where the high plasma rotation (~ 10 kHz near $q = 2$) is maintained. Less peaks are observed in both FFT and PSD spectra, compared to the swept AC vacuum shots such as 131610. More interestingly, the noise level is increased by about factor of 2 compared to the vacuum case, reaching the RMS value of 0.818G for this case.

A similar noise level (RMS=0.779G) is observed for another high beta discharge 130640, although this discharge has a slow plasma flow which is most relevant to the ITER regime. More peaks in FFT, and broader PSD spectrum, are observed in this slow rotation plasma.

We also analyzed a case (140035) that utilizes model-based RWM state-space control [46, 47], again with relatively rapid plasma flow. Even though the FFT and PSD spectra are similar to that of the PID control case 129283, the $n = 1$ high frequency noise level in the state-space control discharges is significantly lower: the RMS is 0.266G for discharge 140035. In fact,

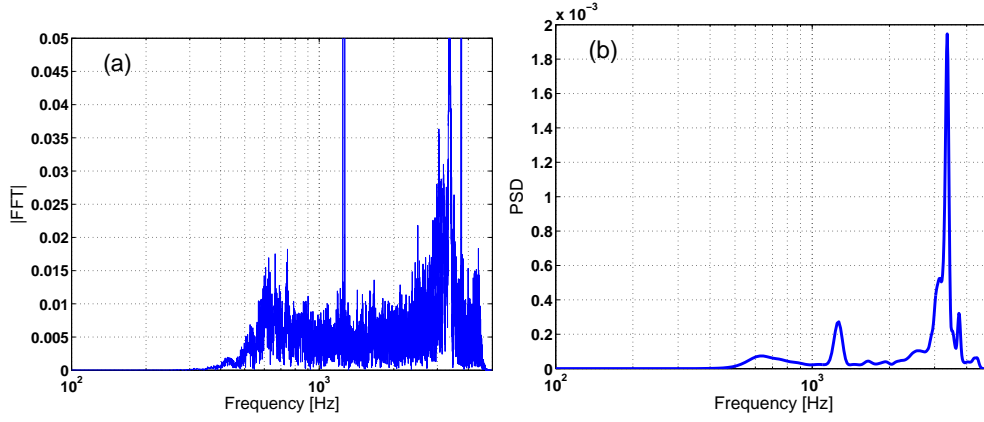


Figure 14: Characteristics of the $n = 1$ noise after applying the Butterworth high-pass filter to the sensor signal in NSTX high beta discharge 129283: (a) the FFT spectrum and (b) the power spectral density of the filtered signal.

this noise level is lower than that found in vacuum shots (with the feedback system not used) by almost a factor of two. This is the lowest level among any cases tested.

4 Results and prediction for ITER

4.1 Summary of all data from various devices

Here we collect and plot the high frequency noise RMS and the bandwidth characteristics for all the data analysed across machines. We consider both the raw voltage data and the time-integrated magnetic field data. The latter have a more complete database.

Figures 15-17 summarise all of the processed voltage signal data presented in previous subsections, from DIII-D, ASDEX Upgrade, and JT-60U plasmas. The DIII-D pickup coil data are grouped into low beta (D3DLM) and high beta (D3DHM) cases. Similar separation is made also for the JT-60U data. The sampling frequency in this database covers about two orders of magnitude.

The RMS data can roughly be grouped into two levels. The lower level, at about 10 Gauss/second, characterises the high frequency noise from the saddle loop data for both ASDEX Upgrade and JT-60U. The high level noise, with RMS varying around $10^4 - 10^5$ Gauss/second, comes from the pickup coils for both DIII-D and JT-60U.

Contrary to the scattering of the RMS data, the bandwidth of the noise signal has a more consistent behaviour as shown in Figs. 16-17. The lower band cut-off frequency, as well as the frequency corresponding to the first peak of the PSD, scales roughly linearly with the data sampling frequency, and the same scaling applies for all types of sensor signals. For

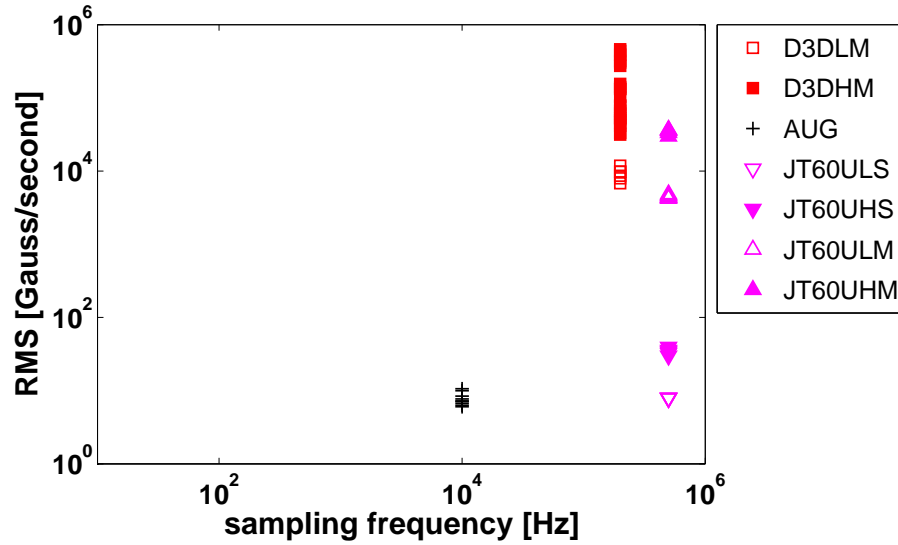


Figure 15: The RMS of the high-frequency noise versus the sampling frequency of the voltage sensor signal, from various present tokamak devices, with legend denoting: D3DLM - DIII-D pickup coil data (b_p) in low beta plasmas; D3DHM - DIII-D pickup coil data (b_p) in high beta plasmas; AUG - ASDEX-Upgrade saddle loop (b_r) data at both low and high beta; JT60ULS - JT-60U saddle loop data (b_r) in low beta plasmas; JT60UHS - JT-60U saddle loop data (b_r) in high beta plasma; JT60ULM - JT-60U pickup coil data (b_p) in low beta plasmas; JT60UHM - JT-60U pickup coil data (b_p) in high beta plasmas.

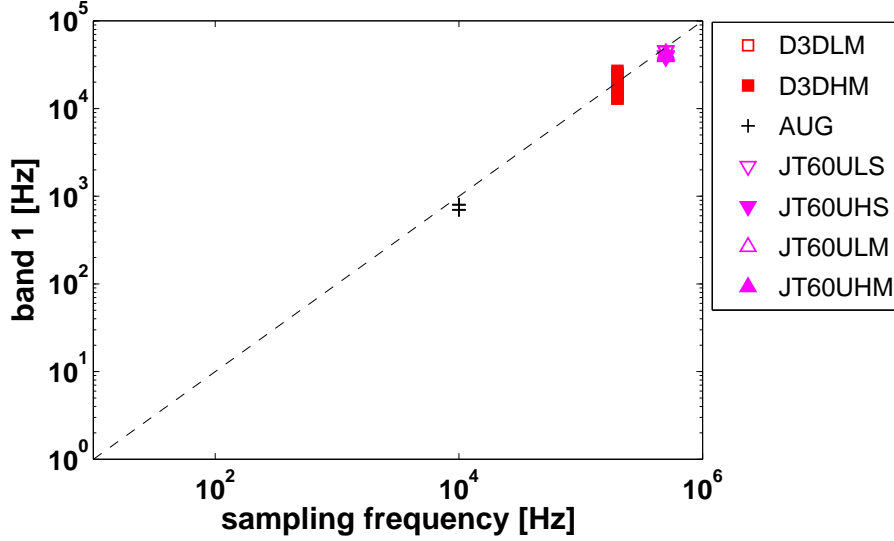


Figure 16: The lower band cut-off frequency of the high-frequency noise versus the sampling frequency of the voltage sensor signal, from various present tokamak devices, with the same legend notations as in Fig. 15. The dashed line corresponds to $y = 0.1x$.

the cut-off frequency, the scaling factor is about 0.1. In other words, the cut-off frequency is expected to be a function of the sampling frequency. We emphasise that the scaling factor of 0.1 here depends on how we select the stopband and the passband of the high-pass filter. With the normalized (by π) stopband of $\omega_s = 0.125$ in the Butterworth filter, the theoretical cut-off frequency of the filtered signal is $0.125\pi/(2\pi) = 0.0625$ per sample, which is close to the estimated scaling factor of 0.1 from the dataset. Similarly, the scaling factor of 0.2, found from the dataset for the higher band frequency as shown in Fig. 17, roughly corresponds to the normalized passband of $\omega_p = 0.25$ chosen for the Butterworth filter. In this work, we select these bands in such a way that the filtered noise signal most likely to have a Gaussian distribution.

Figures 18-20 summarise all the processed field data noise characteristics from DIII-D, JET, ASDEX Upgrade, MAST, JT-60U, and NSTX plasmas. Again we try to distinguish between the vacuum, low beta or high beta plasmas in this database, as well as between the saddle loop and pickup coil data. The sampling frequency in this database covers more than three orders of magnitude.

The field noise level shown in Fig. 18 can again be roughly grouped into two ranges. The low level range covers from $\sim 10^{-5}\text{G}$ to $\sim 10^{-3}\text{G}$. The corresponding signals are mainly picked up by large saddle loops (in ASDEX Upgrade and JT-60U). The high level noise covers the range of $\sim 10^{-2} - 1\text{G}$. Almost all devices included in this study (except ASDEX Upgrade) observe the noise level in this range. Two other general observations are: (i) the pickup coil data (b_p) is always significantly more noisy than the saddle loop data (b_r). This is partially associated with the fact that the b_r sensors are usually mounted on the vacuum vessel wall or some other conducting structure, which should shield them against high frequency fields from inside or outside the vessel. The b_p sensor, on the other hand, should be more sensitive to

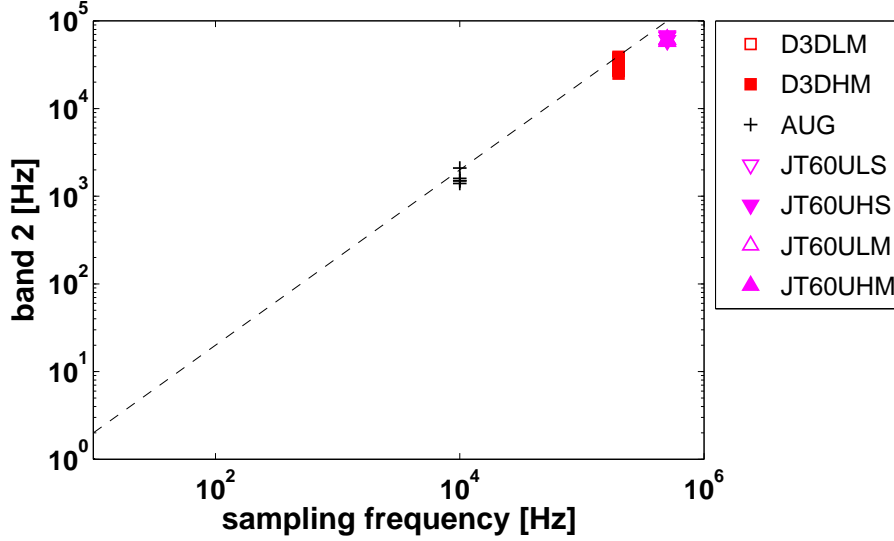


Figure 17: The higher band frequency corresponding to the first peak of the power spectral density, of the high-frequency noise versus the sampling frequency of the voltage sensor signal, from various present tokamak devices, with the same legend notations as in Fig. 15. The dashed line corresponds to $y = 0.2x$.

high frequency signals from the plasma. Note that this statement is true for a given device, but may not always hold across machines. For instance, the high beta b_r signal in MAST has a comparable RMS level to that of the b_p signal in other devices. (ii) the low beta or vacuum data is generally less noisy than the high beta data. The slight exception (in the scale of Fig. 18) is the NSTX high beta data from the state-space control, which produces smaller sensor signal high frequency noise even than the vacuum signal.

The bandwidth characteristics of the field data noise again have a consistent behaviour as shown in Figs. 19-20, largely independent of the device as well as the pickup coils. The lower band cut-off frequency scales roughly linearly with the data sampling frequency, with the scaling factor of about 0.1. The frequency corresponding to the first peak of the PSD, also scales well with the sampling frequency, with a coefficient of ~ 0.2 . As mentioned before, these scaling factors are mainly determined by the choice of the passband and stopband of the Butterworth filter.

Because the bandwidth frequencies (band 1 and 2) linearly scale with the sampling frequency (with a fixed passband and stopband), we may obtain a rather high frequency bandwidth, compared to the typical RWM frequency, if the sampling frequency is high. In principle, it is possible to obtain the noise components with lower bandwidth frequencies, by tuning the passband and stopband of the Butterworth filter for each raw data signal individually. This approach, however, suffers two disadvantages. (i) We lose a uniform criterion for extracting the noise component, and hence a common base for comparing the noise characteristics across various devices, or even in the same device but for raw data measured at different sampling rates. Consequently, the database, obtained this way, may not be useful for extrapolating to ITER. (ii) The filtered signal may not have Gaussian characteristics, resulting in a more

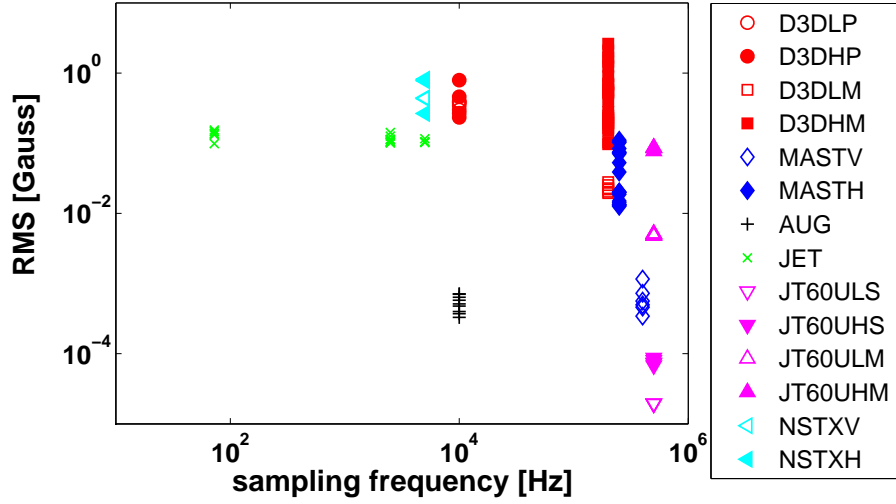


Figure 18: The RMS of the high-frequency noise versus the sampling frequency of the integrated (field) signal, from various present tokamak devices, with legend denoting: D3DLP - DIII-D pickup coil data (b_p) in low beta plasmas; D3DHP - DIII-D pickup coil data (b_p) in high beta plasmas; D3DLM - DIII-D pickup coil data (b_p) in low beta plasmas; D3DHM - DIII-D pickup coil data (b_p) in high beta plasmas; MASTV - MAST vacuum data; MASTH - MAST high beta plasma data; AUG - ASDEX-Upgrade saddle loop (b_r) data at both low and high beta; JET - JET saddle loop (b_r) data in both vacuum and low and high beta plasmas; JT60ULS - JT-60U saddle loop data (b_r) in low beta plasmas; JT60UHS - JT-60U saddle loop data (b_r) in high beta plasma; JT60ULM - JT-60U pickup coil data (b_p) in low beta plasmas; JT60UHM - JT-60U pickup coil data (b_p) in high beta plasmas; NSTXV - NSTX vacuum data; NSTXH - NSTX data in high beta plasmas.

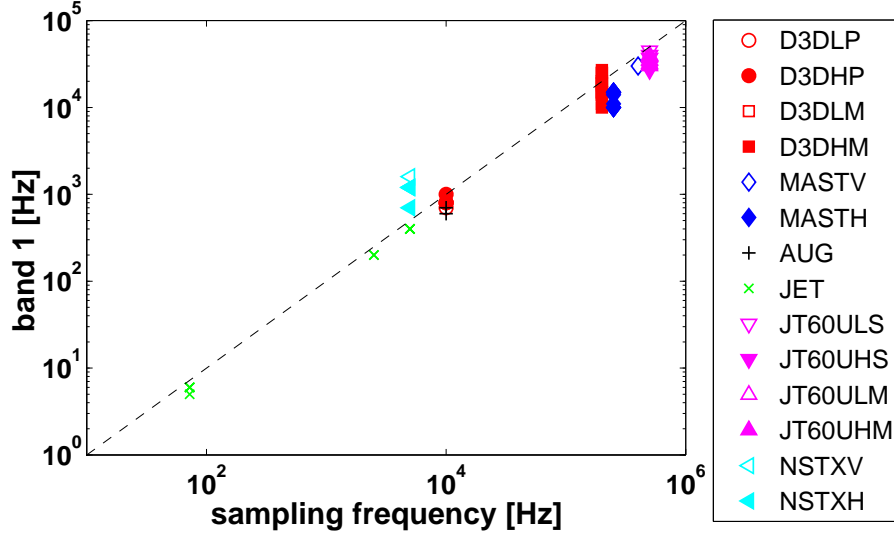


Figure 19: The lower band cut-off frequency of the high-frequency noise versus the sampling frequency of the integrated (field) signal, from various present tokamak devices, with the same legend notations as in Fig. 18. The dashed line corresponds to $y = 0.1x$.

sophisticated way of specifying the noise. This in turn complicates the controller design using, for example, the Kalman Filter which normally assumes Gaussian noise.

We also investigated the dependence of the noise RMS on basic plasma parameters, such as the major radius, the toroidal equilibrium magnetic field, the plasma current, the plasma density, as well as the thermal ion or electron temperature. By re-plotting the database shown in Fig. 18 against the aforementioned parameters, we did not find any clear dependence on these basic parameters. The most prominent feature is still the two-range structure for the RMS level, similar to that shown in Fig. 18.

4.2 Prediction of sensor signal noise for ITER

Based on the results obtained so far for DIII-D, JET, MAST, ASDEX Upgrade, JT-60U and NSTX, we make a prediction for the possible high-frequency noise characteristics in ITER plasmas.

Both figures 15 and 18 show two characteristic ranges of the high frequency noise RMS, for the voltage and field signals respectively. Whilst there is evidence that large saddle loops may significantly reduce the noise level, this may not always be the case (e.g. in JET due to possibly the hardware noise). Therefore, following a conservative approach, we can take the high-value RMS range for extrapolation to ITER. This range is about $10^4 - 10^5$ Gauss/second of the high frequency noise level for the voltage sensor signal, and about 0.1-1G range for the perturbed magnetic field signal. Note that these ranges hold across a wide variation of the plasma conditions and the machine configurations (e.g. in terms of R_0, B_0, I_p), as well

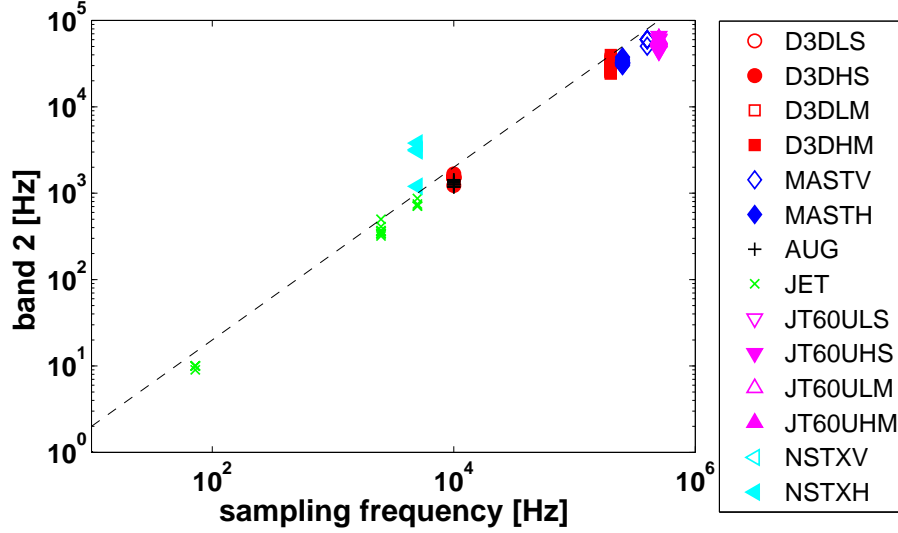


Figure 20: The higher band frequency corresponding to the first peak of the power spectral density, of the high-frequency noise versus the sampling frequency of the integrated (field) signal, from various present tokamak devices, with the same legend notations as in Fig. 18. The dashed line corresponds to $y = 0.2x$.

as across a wide range of the signal sampling frequency. This may indicate that there is a common basis for the high-frequency, Gaussian-like, $n = 1$ noise in tokamak devices.

The bandwidth characteristics of the high frequency noise is very similar between the voltage and the field signals, as shown in Figs. 16-17, 19-20. Whilst these bands (i.e. band 1 and band 2 as defined in this study) depends on the choice of the high pass filter. For the Butterworth filter tested in this work, there is a linear scaling of the bands versus the signal data sampling frequency. We emphasise again that our choice of the high pass filter is partially motivated by the desire of obtaining as close as possible a Gaussian pdf for the filtered signal. Assuming that the same type of filter can be implemented in ITER, the bandwidth characteristics (e.g. the cut-off frequency) of the high-frequency noise in ITER should mainly scale with the signal sampling rate, and the scaling factor of 0.1 may be a reasonable estimate for the cut-off frequency. The lower cut-off frequency may also suggest a way to avoid the high frequency noise in ITER, by tuning the signal sampling frequency. For instance, by choosing a sampling frequency of 10kHz, the lower cut-off frequency for the high frequency Gaussian-like noise should be about 1kHz, according to this database scaling. If we apply a low-pass filter for the RWM sensor signal, with the cut-off frequency below 1kHz (which should be a reasonable assumption for ITER, at least for plasmas that are well below the ideal-wall beta limits), we can effectively eliminate the high frequency noise.

We list some caveats associated with the above predictions:

- Within the present database, we still have a considerable scattering of the noise RMS. In some cases, this scattering may be reduced, or at least understood, by carefully looking into how the sensor signals are measured and processed on each specific device.

Table 4: Parameter ranges of the present database compared with ITER.

	$\sim\text{min}$	$\sim\text{max}$	ITER
$R_0[\text{m}]$	0.8	3	6.2
$B_0[\text{T}]$	0.4	2	5.3
$I_p[\text{MA}]$	0.5	2	9

- Even though the JET data show a consistent RMS independent of the sampling time, we suspect that the high-frequency noise in JET is mostly due to the hardware noise, not due to the plasma generated noise.
- The global machine parameters (R_0, B_0, I_p) cover a wide range by the considered devices. But obviously a significant extrapolation has to be made for the ITER prediction. So far we have not yet established a proper extrapolation law (we just based on the fact that there is no obvious scaling of the noise RMS on the machine parameters). Table 4 lists typical parameter ranges covered by the present database, compared with the ITER parameter for the 9MA steady state Scenario, for which we are mostly interested in the RWM control.

With the predicted noise characteristics for ITER, the next step is to incorporate the sensor signal noise into the RWM feedback modelling codes, in order to investigate how the noise affects the control performance in ITER.

In the feedback simulation, a time series of the noise can be easily generated, giving the following global characteristics: (i) the noise has a Gaussian pdf; (ii) the RMS is known (say between $10^4 - 10^5$ Gauss/second for the voltage signal, or between 0.1-1 Gauss for the field signal); (iii) the cut-off frequency is specified ($0.1 \times$ the sampling frequency of the pickup coil in ITER).

Usually, the above information (i) and (ii) are automatically assumed in a LQG type of control algorithm with Kalman Filter. For a PID type of controller (in state space control), the sensor signal noise, in the form of a time series and satisfying the above conditions (i-iii), need to be explicitly generated and injected into the closed loop simulation.

We also make a short comment here on the pdf of the noise distribution. In this work, we find that the high-pass Butterworth filter generally yields a Gaussian-like pdf. Therefore, we specify the high-frequency noise as a Gaussian signal for ITER. Another possible choice of the noise model is the white noise with a uniform pdf. On the other hand, application of the high-pass Butterworth filter to a white noise also produces a Gaussian-like pdf, meaning that a Gaussian noise is probably a better noise model for the purpose of modelling the RWM control, assuming that a filtered signal is to be used for the sensor signal in the feedback loop.

5 Summary

We have developed a procedure (NSAT) for systematic analysis of the high frequency magnetic pickup signal noise. This noise may affect the performance of feedback systems applied for the purpose of controlling the low- n ($n = 1$ in this work) RWM. The analysis has been applied to various present day tokamak devices (JET, DIII-D, MAST, ASDEX Upgrade, JT-60U, NSTX), resulting in a cross-machine database for the sensor signal noise. We focus on characterising the noise component that satisfies the Gaussian distribution. To achieve this, we apply a high-pass Butterworth filter to the raw sensor signals. Both FFT and PSD analysis are then performed on the filtered signals.

The RMS level of the high frequency noise significantly varies across the machines, as well as in the same machine but at different plasma conditions and signal sampling frequencies. Generally the plasma tends to enhance the noise level, often by orders of magnitude, compared to the vacuum noise. The noise level in high beta plasmas is higher than that in low beta plasmas. One exception is JET, where the noise seems to be predominantly produced by hardware (the analogue-digital converter). The noise level also changes with the feedback configurations (DIII-D and NSTX), although the variation is less significant compared to other factors. For the assembled database, after application of the Butterworth filter, the largest high frequency noise is of order $10^4 - 10^5$ Gauss/second for the voltage signal, and 0.1-1 Gauss for the perturbed magnetic field signal, which we suggest as a conservative estimate for ITER.

The analysis, based on the NSAT unified framework, reveals a systematic linear scaling of the cut-off frequencies for the high frequency noise, as a function of the signal sampling frequency. This is inherently related to the properties of the chosen filter. The coefficient for the lower cut-off frequency is about 0.1, indicating that the lower cut-off frequency should be in the kHz level in ITER, provided that the sensor signal sampling frequency for the RWM is in the tens of kHz range. Such a high frequency noise component may be important for high beta plasmas in ITER steady state scenarios, in particular when the plasma pressure approaches the ideal wall beta limit. At lower beta, this high frequency component can in principle be removed by applying a low-pass filter to the sensor signal, with upper cut-off frequency below the kHz level.

For the future, it is desirable to further expand the database created during this study, by including more devices, and/or analysing more discharges within the existing devices. Eventually, the above characteristics (Gaussian distribution, RMS, bandwidth) can be used to generate sensor signal noise components for predictive modelling of the RWM control in ITER plasmas, which is part of our future work.

Acknowledgements. This project has received funding from the European Union’s Horizon 2020 research and innovation programme under grant agreement number 633053 and from the RCUK Energy Programme [grant number EP/I501045] and the US department of energy under DE-AC02-09CH11466, DE-DE-FC02-04ER54698 and DE-FG02-99ER54524. The views and opinions expressed herein do not necessarily reflect those of the European Commission and ITER Organization.

References

- [1] Bondeson A and Ward D J 1994 *Phys. Rev. Lett.* **72** 2709
- [2] Sabbagh S A et al 2006 *Nucl. Fusion* **46** 635
- [3] Boozer A H, 2001 *Phys. Rev. Lett.* **86** 22
- [4] Hender T C et al 2007 *Nucl. Fusion* **47** S128
- [5] Sabbagh S A et al 2006 *Phys. Rev. Lett.* **97** 045004
- [6] Chu M S and Okabayashi M 2010 *Plasma Phys. Control. Fusion* **51** 123001
- [7] Igochine V 2012 *Nucl. Fusion* **52** 074010
- [8] Villone F et al 2010 *Nucl. Fusion* **50** 125011
- [9] Betti R 1995 *Phys. Rev. Lett.* **74** 2949
- [10] Chu M S et al 1995 *Phys. Plasmas* **2** 2336
- [11] Bondeson A and Chu M S 2006 *Phys. Plasmas* **3** 3013
- [12] Hu B and Betti R 2004 *Phys. Rev. Lett.* **93** 105002
- [13] Liu Y Q et al 2005 *Nucl. Fusion* **45** 1131
- [14] Zheng L J et al 2005 *Phys. Rev. Lett.* **95** 25503
- [15] Liu Y Q et al 2008 *Phys. Plasmas* **15** 092505
- [16] Liu Y Q et al 2008 *Phys. Plasmas* **15** 112503
- [17] Chapman I T 2009 *Plasma Phys. Controlled Fusion* **51** 055015
- [18] Berkery J W et al 2010 *Phys. Rev. Lett.* **104** 035003
- [19] Berkery J W et al 2010 *Phys. Plasmas* **17** 082504
- [20] Sabbagh S A et al 2010 *Nucl. Fusion* **50** 025020
- [21] Hao G Z et al 2011 *Phys. Rev. Lett.* **107** 015001
- [22] Berkery J W et al 2011 *Phys. Rev. Lett.* **106** 075004
- [23] Berkery J W et al 2014 *Phys. Plasmas* **21** 056112
- [24] Garofalo A M et al 1999 *Phys. Rev. Lett.* **82** 3811
- [25] La Haye R J et al 2004 *Nucl. Fusion* **44** 1197
- [26] Reimerdes H et al 2007 *Phys. Rev. Lett.* **98** 055001
- [27] Takechi M et al 2007 *Phys. Rev. Lett.* **98** 055002

- [28] Strait E J et al 2007 *Phys. Plasmas* **14** 056101
- [29] Gryaznevich M P et al 2008 *Plasma Phys. Control. Fusion* **50** 124030
- [30] Okabayashi M et al 2011 *Phys. Plasmas* **18** 056112
- [31] Matsunaga G et al 2013 *Nucl. Fusion* **53** 123022
- [32] Fitzpatrick R and Jensen T H 1996 *Phys. Plasmas* **3** 2641
- [33] Okabayashi M et al 1998 *Nucl. Fusion* **38** 1607
- [34] Liu Y Q and Bondeson A 2000 *Phys. Rev. Lett.* **84** 907
- [35] Liu Y Q et al 2000 *Phys. Plasmas* **7** 3681
- [36] Pustovitov V D 2001 *Plasmas Phys. Rep.* **27** 195
- [37] Bialek J et al 2001 *Phys. Plasmas* **8** 2170
- [38] Bondeson A et al 2002 *Nucl. Fusion* **42** 768
- [39] Chu M S et al 2003 *Nucl. Fusion* **43** 441
- [40] Liu Y Q et al 2006 *Phys. Plasmas* **13** 056120
- [41] Strumberger E et al 2008 *Phys. Plasmas* **15** 056110
- [42] Pustovitov V D 2008 *Plasma Phys. Control. Fusion* **50** 105001
- [43] Okabayashi M et al 2005 *Nucl. Fusion* **45** 1715
- [44] Okabayashi M et al 2009 *Nucl. Fusion* **49** 125003
- [45] In Y et al 2010 *Plasma Phys. Control. Fusion* **52** 104004
- [46] Sabbagh S A et al 2011 *Proceedings of the 38th European Conference on Plasma Physics, Strasbourg, France, 27 Jun C 1 Jul 2011 (EPS, Petit-Lancy, Switzerland)* paper P5.104
- [47] Sabbagh S A et al 2013 *Nucl. Fusion* **53** 104007
- [48] Liu Y Q et al 2009 *Nucl. Fusion* **49** 035004
- [49] Liu Y Q 2010 *Nucl. Fusion* **50** 095008
- [50] Chapman I T et al 2012 *Phys. Plasmas* **19** 052502
- [51] Liu Y Q et al 2004 *Nucl. Fusion* **44** 232
- [52] Xia et al 2014 *Plasma Phys. Controlled Fusion* **56** 095009
- [53] Katsuro-Hopkins et al 2007 *Nucl. Fusion* **47** 1157
- [54] G.Ambrosino, et al., Plasma position and shape control for ITER scenarios, December 2007, EFDA private communications.

- [55] Liu Y Q et al 2014 *Report to ITPA MHD Topical Group on WG-7: Resistive wall feedback control*
- [56] Gerasimov S N et al 2014 *Nucl. Fusion* **54** 073009